INORGANIC CHEMISTRY FRONTIERS

RESEARCH ARTICLE

View Article Online
View Journal | View Issue

Cite this: *Inorg. Chem. Front.*, 2025, **12**, 7342

High-sensitivity lanthanide ratiometric nanothermometers in the second biological window through bidirectional thermal response engineering†

Shuohan Sun, [a] Dekang Huang,[a] Dan Li,[b] Mochen Jia[c] and Guanying Chen *[b]

In recent years, lanthanide-doped nanothermometers have made significant progress as non-contact temperature sensing tools in a variety of biological fields. However, limited successes have been met in high-sensitivity nanothermometers operating in the second near-infrared (NIR-II) biological window, which can enable sub-centimeter tissue penetration at micrometer-level imaging resolutions. Here, we adopted a core–shell structure to develop a high-sensitivity lanthanide ratiometric nanothermometer through a bidirectional thermal response of two emissions peaks in the NIR-II window. We showed that, under 808 nm excitation, the emission intensity at 1330 nm from neodymium ions exhibited a quenching effect, while the one at 1565 nm from erbium ions showed an enhancement at elevated temperatures. This contrasted temperature dependency endows the nanothermometer with a high relative sensitivity above 2.3% °C^{-1}, with a maximum of 2.5% °C^{-1}, throughout the entire physiological temperature range (30–45 °C). This high-sensitivity nanothermometer enables reliable differentiation of temperature differences in both normal and inflamed mice, highlighting its promising uses for *in vivo* applications.

Received 29th April 2025,
Accepted 17th July 2025

DOI: 10.1039/d5qi01027f

rsc.li/frontiers-inorganic

Introduction

In living organisms, even slight temperature fluctuations can impact various biological processes.[1,2] Yet, traditional contact thermometers are not suitable for *in vivo* temperature monitoring because their invasiveness and limited spatial resolution make it difficult to detect subtle thermal changes. This limitation has led to growing interest in advanced non-invasive nanothermometers that can provide high-resolution measurements without disturbing the biological system.[3,4] Within this array of technologies, employing a luminescent nanothermometer has emerged as a highly precise remote temperature measurement method, with the potential to provide detailed temperature imaging distribution within deep tissue.[5,6]

Among the various luminescent nanoprobes studied, lanthanide-doped nanoparticles are particularly attractive due to their narrow, rich emission peaks and inherent resistance to external environmental interference.[7,8] Among them, the commonly used types are ratiometric and lifetime nanothermometers. Although lifetime nanothermometers possess the unique advantage of being unaffected by tissue coverage, they exhibit slower detection speed, necessitate more expensive experimental equipment, and require the involvement of subsequent calculations. In contrast, ratiometric nanothermometers provide a self-referencing mechanism that minimizes external perturbations and offer a rapid response time, thereby attracting extensive interest.[9–11] Traditionally, ratiometric nanothermometers have relied on thermally coupled energy levels,[12] such as the extensively studied $^{2}H_{11/2}$ and $^{4}S_{3/2}$ level pairs of the Er^{3+} ion.[13,14] However, the limited energy gap of these levels (200–2000 cm^{-1}) restricts further improvement of their relative sensitivity.[15] In contrast, nanothermometers based on nonthermally coupled energy levels offer the potential for higher sensitivity.[16–18] Specifically, when doping with different activator ions, selecting two emission peaks that vary oppositely with temperature, where one peak is thermally enhanced and the other undergoes thermal quenching, facilitates the achievement of higher relative sensitivity.

What's more, it is well known that the near-infrared (NIR) biological windows can be divided into NIR-I (650–950 nm)

[a]*School of Chemistry, Huazhong Agricultural University, Wuhan 430070, China*
[b]*MIIT Key Laboratory of Critical Materials Technology for New Energy Conversion and Storage, School of Chemistry and Chemical Engineering & Key Laboratory of Micro-systems and Micro-structures, Ministry of Education, Harbin Institute of Technology, Harbin 150001, China. E-mail: chenguanying@hit.edu.cn*
[c]*Key Laboratory of Materials Physics of Ministry of Education, School of Physics, Zhengzhou University, Zhengzhou 450052, China*

†Electronic supplementary information (ESI) available: Characterization, XRD patterns, FT-IR spectra, temperature measurement parameters and fitting parameters and temperature-dependent spectra. See DOI: https://doi.org/10.1039/d5qi01027f

and NIR-II (1000–1700 nm). The weaker light scattering and molecular absorption effects within these windows help achieve deeper penetration depth, improve the accuracy of temperature measurements, and enhance imaging resolution.[19,20] In particular, detection windows with wavelengths exceeding 1400 nm have been shown to achieve superior signal-to-noise ratios and deeper tissue penetration.[21–25] Notably, Skripka *et al.* selected emission wavelengths of 1340 nm and 1550 nm, achieving a maximum relative sensitivity of 1.1% $°C^{-1}$.[26] Moreover, Maciejewska *et al.* synthesized $LaPO_4$:1%Nd^{3+},20%Er^{3+} nanocrystals as ratiometric nanothermometers, employing the ratio of luminescence intensities at 1055 nm and 1540 nm and achieving a maximum relative sensitivity of 1.15% K^{-1}.[27] Despite these advances, strategies for the improvement of the relative sensitivity of nanothermometers operating in the NIR-II window remain elusive.[28–30]

In this work, we synthesized $NaYF_4$:Er^{3+}/Ce^{3+}@$NaYbF_4$@$NaYF_4$:Nd^{3+}/Yb^{3+} nanoparticles (abbreviated as NPs), whose emission peaks in the NIR-II region exhibit opposite responses to temperature under 808 nm laser excitation. As the temperature increases, the emission peak of Er^{3+} (1565 nm) exhibits thermal enhancement, whereas the emission peak of Nd^{3+} (1330 nm) undergoes thermal quenching. Based on these two emission peaks, a ratiometric nanothermometer was constructed, and its relative sensitivity was further optimized by adjusting the doping ratios of Nd^{3+} and Er^{3+}. The NPs were further surface-modified with polyacrylic acid (PAA) to improve biocompatibility and were successfully employed to monitor temperature changes in a mouse model of subcutaneous inflammation. The ratiometric nanothermometer, exhibiting bidirectional temperature-dependent emission in the NIR-II region, shows great potential for monitoring temperature changes *in vivo*.

Results and discussion

$NaYF_4$:Er^{3+}/Ce^{3+}@$NaYbF_4$@$NaYF_4$:Nd^{3+}/Yb^{3+} was synthesized *via* a seed-mediated layer-by-layer method using high-temperature thermal decomposition of metal trifluoroacetates.[31,32] The transmission electron microscopy (TEM) image of $NaYF_4$:Er^{3+}/Ce^{3+} (core) was obtained, confirming the successful synthesis of homogeneous spherical cores (6.9 nm) (Fig. 1a and d). Subsequently, the cores were coated with an $NaYbF_4$ shell layer of about 4.5 nm thickness as an energy transport layer, followed by an outermost $NaYF_4$:Nd^{3+}/Yb^{3+} shell layer (about 6.5 nm in thickness) functioning as both a sensitizer layer and an activator layer (Fig. 1b, c, e and f). Both shell layers were applied using the epitaxial growth method. The measured X-ray powder diffraction (XRD) pattern compared with the standard card also proved the successful synthesis of $NaYF_4$, which exhibited a hexagonal crystal phase (Fig. S1†). Next, to enhance the biocompatibility of the NPs, we modified the nanocrystal surfaces with PAA. This modification was confirmed using Fourier transform infrared (FTIR) spectroscopy

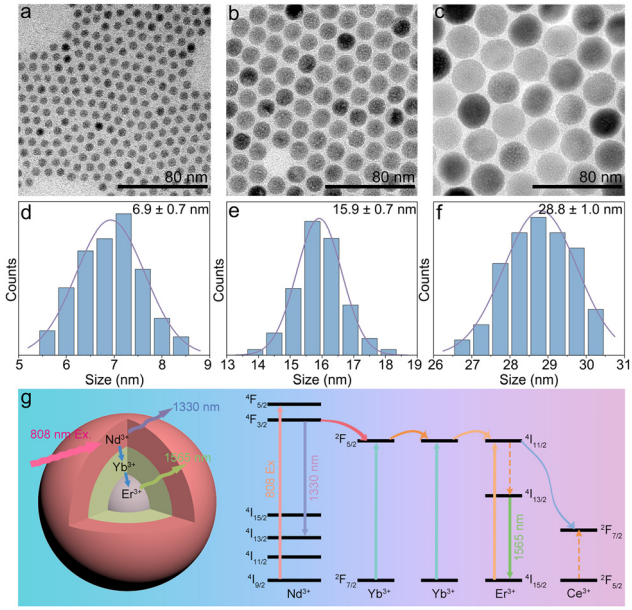

Fig. 1 TEM image and particle size distribution of the (a and d) $NaYF_4$:Er^{3+}/Ce^{3+} core, (b and e) $NaYF_4$:Er^{3+}/Ce^{3+}@$NaYbF_4$ core–shell and (c and f) $NaYF_4$:Er^{3+}/Ce^{3+}@$NaYbF_4$@$NaYF_4$:Nd^{3+}/Yb^{3+} core–shell–shell. (g) The simplified energy diagrams of Nd^{3+}, Yb^{3+}, Er^{3+} and Ce^{3+} ions in the core–shell–shell structure, along with the energy transfer processes.

(Fig. S2†). Initially, the surface coated with oleic acid exhibited the asymmetric and symmetric bending modes of the carboxylic group at 1465 and 1560 cm^{-1}, along with the asymmetrical and symmetrical stretching modes of the methylene group at 2855 and 2926 cm^{-1}. After coating with PAA, these peaks were replaced by the C=O stretching mode at 1656 cm^{-1}.[33] Additionally, to evaluate the stability of the NPs in a biological environment, we dispersed the PAA-modified NPs in phosphate-buffered saline (PBS) and measured their hydrodynamic diameter using dynamic light scattering (DLS). After being stored for half a month, the DLS measurement was repeated, and no significant change in the hydrodynamic diameter was observed (Fig. S3†). Moreover, the solution remained clear without any visible aggregation, demonstrating that the NPs can remain stable in PBS. Therefore, all subsequent tests were conducted in an aqueous system.

For the study of luminescence performance, we first tested the absorption spectrum of NPs, NPs have a strong absorption peak at 800 nm (Fig. 2a). Next, when Nd^{3+} is excited by an 808 nm laser, the electrons first transition from the ground state ($^4I_{9/2}$) to the excited state ($^4F_{5/2}$). They then undergo a non-radiative relaxation process to the $^4F_{3/2}$ energy level (Fig. 1g). From there, it can emit fluorescence around 1330 nm through radiative relaxation to the $^4I_{13/2}$ level, or transfer energy to $^2F_{5/2}$ (Yb^{3+}) through phonon-assisted processes. Then, Yb^{3+} acts as a bridging ion facilitating energy transfer between the two shell regions. Then, energy migrates through the transfer layer to $^4I_{11/2}$ (Er^{3+}), followed by a non-radiative resonance energy transfer to the $^4I_{13/2}$ level. Finally, $^4I_{13/2}$ (Er^{3+})

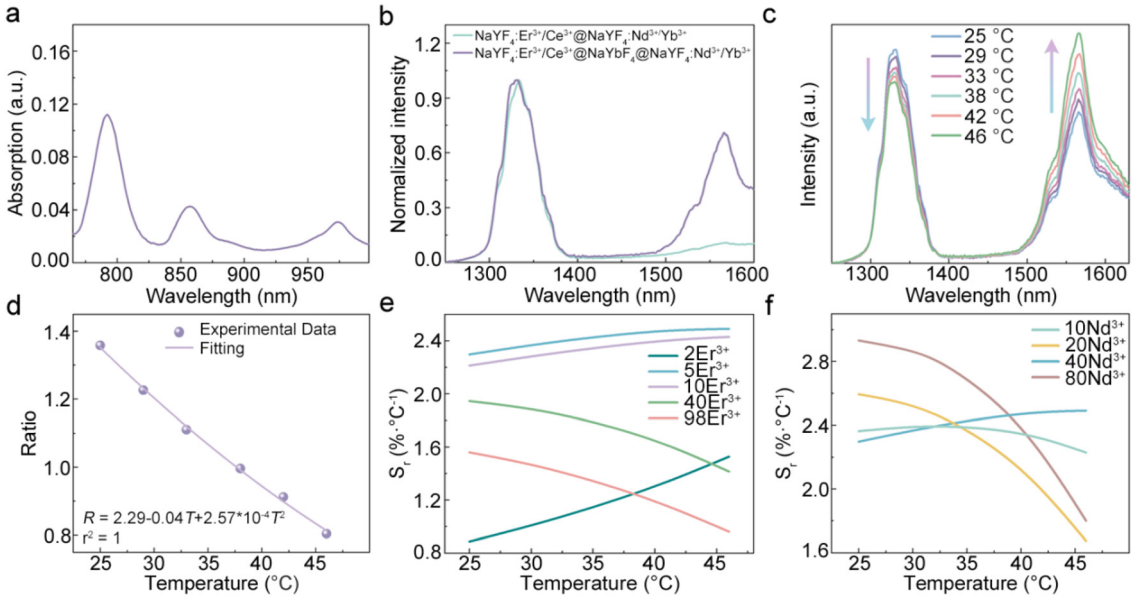

Fig. 2 (a) Absorption spectra of the NPs. (b) Normalized emission spectra of $NaYF_4$:5Er^{3+}/2Ce^{3+}@$NaYF_4$:40Nd^{3+}/20Yb^{3+} and $NaYF_4$:5Er^{3+}/2Ce^{3+}@$NaYbF_4$@$NaYF_4$:40Nd^{3+}/20Yb^{3+}. (c) Temperature dependence of the emission spectra of $NaYF_4$:5Er^{3+}/2Ce^{3+}@$NaYbF_4$@$NaYF_4$:40Nd^{3+}/20Yb^{3+}. (d) Temperature dependence of the intensity ratio between the emission at 1330 and 1565 nm. The acquired S_r values of (e) $NaYF_4$,xEr^{3+}/2Ce^{3+}@$NaYbF_4$@$NaYF_4$,40Nd^{3+}/20Yb^{3+} nanoparticles with varied Er^{3+} concentrations and (f) $NaYF_4$,5Er^{3+}/2Ce^{3+}@$NaYbF_4$@$NaYF_4$:yNd^{3+}/20Yb^{3+} nanoparticles with varied Nd^{3+} concentrations. All temperature-dependent spectra were measured in an aqueous environment.

emits fluorescence at 1565 nm. In this structure, we chose the fluoride matrix due to its low phonon energy, which reduces the non-radiative relaxation process to maximize the luminescence intensity. In addition, we explored the impact of the presence of an energy migration layer on the emission peak. It can be observed that the energy migration layer facilitates energy transfer from Nd^{3+} to Er^{3+} *via* Yb^{3+} ions, significantly enhancing the relative intensity of Er^{3+} (Fig. 2b). What's more, we measured the down-conversion quantum yield of the NPs under 808 nm laser excitation, which was determined to be 7.71% (scattering range: 770–840 nm; emission range: 850–1600 nm).

In order to evaluate the thermometric performance of the NPs as a ratiometric nanothermometer, we investigated the relationship between 1330 nm (Nd^{3+}) and 1565 nm (Er^{3+}) with respect to temperature ($R = I_{1330\ nm}/I_{1565\ nm}$). The corresponding temperature-dependent spectra of the nanothermometer are shown in Fig. 2c. With the increase of temperature, the emission at 1330 nm (Nd^{3+}) gradually decreases, while the emission at 1565 nm (Er^{3+}) gradually increases. Therefore, the R value exhibits a gradual decline as the temperature rises (Fig. 2d). This is because the phonon-assisted energy transfer process from Nd^{3+} ($^4F_{3/2}$) to Yb^{3+} ($^2F_{5/2}$) increases with increasing temperature, resulting in the decrease of 1330 nm (Nd^{3+}) fluorescence.[26,34,35] Moreover, the thermal enhancement of Er^{3+} emission arises from the increased vibrational frequency of –OH groups at elevated temperatures, which improves energy matching with the $^4I_{11/2} \rightarrow {}^4I_{13/2}$ (Er^{3+}) transition, while reducing coupling with the $^4I_{13/2} \rightarrow {}^4I_{15/2}$ (Er^{3+}) transition.[26,36] This mechanism is corroborated by the observed prolongation of Er^{3+} emission lifetime with increasing temperature (Fig. S4†). What's more, many studies have shown that the doping of Ce^{3+} is conducive to the enhancement of Er^{3+} 1565 nm down-conversion emission.[37,38] This is attributed to the occurrence of this process: $^4I_{11/2}$ (Er^{3+}) + $^2F_{5/2}$ (Ce^{3+}) → $^4I_{13/2}$ (Er^{3+}) + $^2F_{7/2}$ (Ce^{3+}). The increasing temperature will also further promote this process, thus promoting the thermal enhancement effect of 1565 nm (Er^{3+}). Here, we compared the temperature-dependent 1565 nm lifetimes of Er^{3+} in nanocrystals with and without Ce^{3+} doping (Fig. S4†). We observed a more pronounced increase in lifetime with Ce^{3+} doping, suggesting that the thermal enhancement at 1565 nm arises from the combined effects of changes in the –OH vibrational frequency and Ce^{3+}-induced cross-relaxation processes. In this way, the two emission peaks reverse with the change of temperature, and the ratio of the intensity of the two emission peaks can be used to construct a high-sensitivity nanothermometer.

To make a more reliable comparison, we calculated the relative sensitivity (S_r) to quantitatively evaluate the extent of R variation with temperature. The S_r is calculated using the following formula:

$$S_r = \frac{1}{R}\frac{\partial R}{\partial T} \quad (1)$$

In order to determine the optimal Nd^{3+} and Er^{3+} doping ratio for the core–shell–shell structure to obtain the maximum S_r, we synthesized a series of samples with different Nd^{3+} and Er^{3+} ion-doping ratios and measured their temperature-dependent spectra under 808 nm laser excitation (Fig. S5 and S6†). The relationship between R and temperature for each sample

can be described by using the following polynomial equation (Fig. S7†):

$$R = a + bT + cT^2 \quad (2)$$

where a, b and c are constants. The fitting results are listed in Tables S1 and S2.† All the samples showed a good fitting relationship. When the Nd^{3+} dopant concentration is fixed at 40%, the temperature measurement performance is affected by changes in the Er^{3+} concentration (ranging from 2%, 5%, 10%, and 40% to 98%). It can be seen that variations in the Er^{3+} concentration primarily affect the magnitude of the change in the emission peak at 1565 nm, while the change in the emission intensity at 1330 nm is relatively small (Fig. S8a and b†). This is because the decrease in the Nd^{3+} 1330 nm emission peak is mainly due to the phonon-assisted energy transfer process from $^4F_{3/2}$ (Nd^{3+}) to $^2F_{5/2}$ (Yb^{3+}), which strengthens as the temperature increases, and is almost unaffected by the Er^{3+} doping concentration. As the Er^{3+} doping concentration increases, the extent of the increase at 1565 nm first grows and then decreases. Specifically, the maximum change is 45% at the doping ratio of 5%, while the minimum change is 16% at the doping ratio of 98%. Therefore, the nanothermometer achieves the highest S_r at the Er^{3+} doping concentration of 5% (Fig. 2e).

Then, we fixed the Er^{3+} doping concentration at 5% and varied the Nd^{3+} doping ratios (10%, 20%, 40% and 80%). The effect on the change in the 1330 nm emission of Nd^{3+} and the 1565 nm emission of Er^{3+} is relatively small. The relative sensitivity shows a slight increase with the increase in the Nd^{3+} doping concentration. This is because, when the Yb^{3+} ion concentration is sufficiently high, the increase in the Nd^{3+} ion concentration may enhance the phonon-assisted energy transfer from $^4F_{3/2}$ (Nd^{3+}) to $^2F_{5/2}$ (Yb^{3+}), which facilitates the decrease in the Nd^{3+} emission peak intensity with increasing temperature (with a maximum decrease of 15% at the 80% Nd^{3+} doping ratio) (Fig. S8c†). However, this has a minimal impact on the thermal response characteristics at 1565 nm (Fig. S8d†). That is, the maximum S_r of 2.9% °C^{-1} at 25 °C is achieved when the Nd^{3+} doping concentration is optimized at 80%. However, considering the higher S_r achieved throughout the biological application range, its performance is not as good as that of the sample with an Nd^{3+} doping ratio of 40% (Fig. 2f). It reaches a maximum S_r of 2.5% °C^{-1} at 46 °C, and its S_r remains above 2.3% °C^{-1} throughout the physiological range (30–45 °C). Therefore, for subsequent applications, we continued to use Er^{3+} and Nd^{3+} doping ratios of 5% and 40%, respectively. Here, the S_r of the NPs is also compared with that of other nanothermometers operating in the NIR-II regions (Fig. 3).[26,29,39–42] The NPs have long emission wavelengths and high relative sensitivity values, providing unique advantages for *in vivo* temperature sensing.

For the upcoming *in vivo* applications, we systematically evaluated the potential effects of probe concentration, environmental pH fluctuations, irradiation duration, and excitation power density variations on the temperature measurement

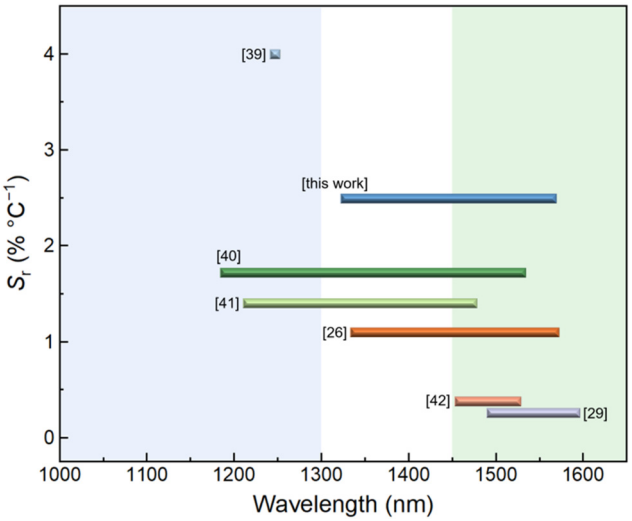

Fig. 3 Comparison of reported S_r values of nanothermometers operating in the NIR-II region.

parameter R. As shown in Fig. 4a and b, changing the probe concentration (0.1–1.6 mg mL^{-1}) and adjusting the solution pH from 5 to 10 had no effect on the R value. Similarly, continuously irradiating the solution with an 808 nm laser for 30 minutes with measurements taken every 5 minutes, as well as varying the excitation power density, did not affect the R value (Fig. 4c and d). More importantly, the stability of the NPs was demonstrated through eight heating and cooling cycles (Fig. 4e). The temperature uncertainty of the NPs was assessed through 20 consecutive tests (Fig. 4f). Using the following temperature uncertainty formula, the obtained temperature uncertainty was 0.15 °C:[43]

$$\delta T = \frac{1}{S_r}\frac{\delta R}{R} \quad (3)$$

Before applying the NPs to the mouse model, we conducted a methyl thiazolyl tetrazolium (MTT) assay on 4T1 cells. The results show that even at a relatively high concentration (640 μg mL^{-1}), the cell viability remains greater than 80%, confirming that the NPs exhibit no significant cytotoxicity and are suitable for biological applications (Fig. S9†). For the upcoming *in vivo* tests, we utilized an InGaAs camera with bandpass filters (1300/1550 nm) to capture the signals. Initially, we established a calibration curve by plotting the R values against temperature for the NPs dispersed in PBS solution (500 μg mL^{-1}) (Fig. 5b). Then, we used 100 μL of yeast solution to induce subcutaneous inflammation in a mouse, which resulted in an increase in subcutaneous temperature. Mice from another group were injected with an equal volume of normal saline as the control group. Equal amounts of PBS solution containing the NPs (500 μg mL^{-1}) were injected into the subcutaneous sites approximately 2 mm deep on the backs of the two mice, and the mice were then left for 12 hours to allow inflammation to develop. Under 808 nm laser excitation (0.1 W cm^{-2}), the fluorescence intensity at the 1330 nm and

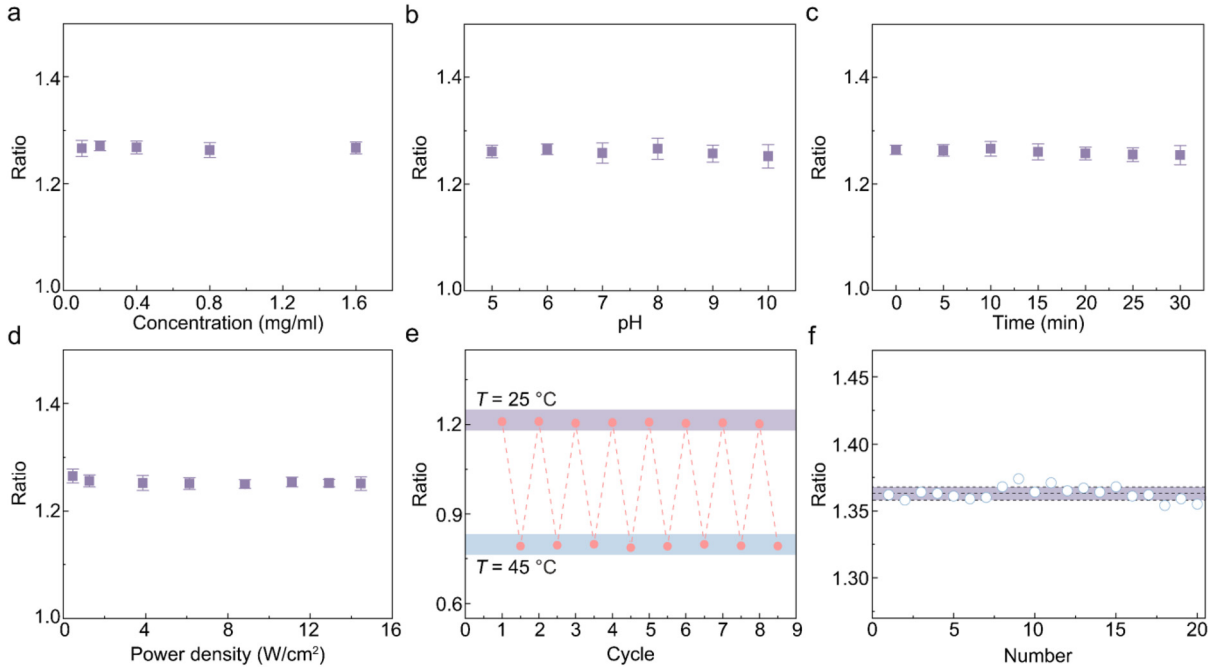

Fig. 4 Stability of R against (a) probe concentration, (b) pH, (c) 30 min of irradiation with an 808 nm laser (10 W cm^{-2}), and (d) fluctuations in the excitation light power density. (e) Repeatability of the ratio of emissions at 1330 and 1565 nm ($R = I_{1330\ nm}/I_{1565\ nm}$) with eight cycles of heating and cooling between 25 and 45 °C. (f) R against continuous measurements.

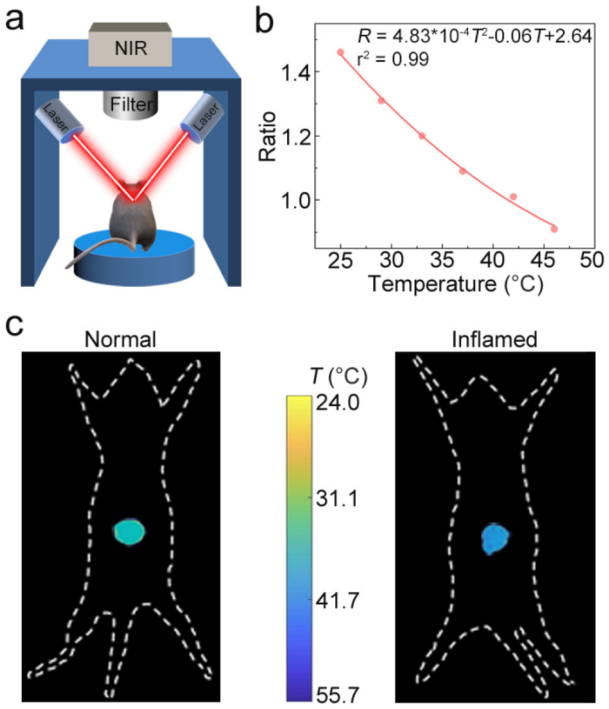

Fig. 5 (a) Schematic diagram of the mouse imaging system. (b) A calibration curve of R acquired using an NIR-sensitive InGaAs camera in combination with appropriate band-pass optical filters. (c) Thermal imaging of the NPs in both normal and inflamed mice, showing precise local temperature distribution around the NPs.

1550 nm signal channels was collected using the aforementioned InGaAs camera coupled with the corresponding optical filters (Fig. 5a). Then, the corresponding R distribution image was obtained through image processing by dividing the former by the latter. Then, based on the previously obtained calibration curve, the subcutaneous temperature distribution information of the two mice was determined from the obtained R. As a result, a clear temperature difference was observed between the groups (Fig. 5c). The subcutaneous temperature in the normal mice (left side) was 36.2 °C, whereas the inflammation group (right side) showed an elevated temperature of 39.3 °C, reflecting a 3.1 °C increase. We also measured the epidermal temperature of the mice using an infrared thermal camera (Fig. S10†), and the temperatures obtained were consistent with those measured when using the NPs. This indicates that NPs can accurately detect the increase in subcutaneous temperature caused by inflammation, demonstrating their promising potential for biomedical applications.

Conclusions

In summary, we developed a nanothermometer with two emission peaks in the NIR-II region, where one peak exhibits thermal enhancement and the other undergoes thermal quenching. As a result, it can achieve a relatively high S_r of up to 2.5% °C^{-1}, and remains above 2.3% °C^{-1} throughout the entire physiological temperature range. We also demonstrated its stability and repeatability through multiple measurements and eight heating–cooling cycles between 25 and 45 °C.

Furthermore, it was modified by PAA to improve its biocompatibility, and applied to a murine model of subcutaneous inflammation, demonstrating that it can effectively monitor temperature changes induced by inflammation. These results highlight the exceptional promise of Nd^{3+}- and Er^{3+}-doped nanocrystals with NIR-II emission peaks for delivering highly accurate temperature measurements in live mammalian systems.

Experimental

Materials

Rare-earth oxides Y_2O_3, Nd_2O_3, and Yb_2O_3, sodium trifluoroacetate (NaTFA), and trifluoroacetic acid (TFA) were purchased from Aladdin Chemistry Co. Ltd. Oleic acid (OA, >90%), oleylamine (OM, >70%), and 1-octadecene (ODE, >90%) were obtained from Sigma-Aldrich Co. Ltd. Hexane and ethanol were purchased from Beijing Chemical Reagents, China. All materials were used as received without further purification.

Synthetic procedures

Synthesis of $NaYF_4$:$x$$Er^{3+}$/2$Ce^{3+}$ core nanoparticles. 1 mmol of rare earth chloride salts ($YCl_3{\cdot}6H_2O$, $ErCl_3{\cdot}6H_2O$ and $CeCl_3{\cdot}6H_2O$) along with 3 mL of H_2O, 3.5 mL of ethanol and 7 mL of hexane were added proportionally to a three-neck flask. The mixture was heated to 60 °C and refluxed for 12 hours. After cooling to room temperature, the water layer was removed and 4 mmol of sodium oleate, 5.2 mL of OA, 5.1 mL of OM, and 9 mL of ODE were added. The reaction mixture was heated to 100 °C under argon and maintained for 1 hour. Then, 4 mmol of NH_4F was added to the reaction mixture and stirred for another half hour. The temperature was then increased to 300 °C over 20 minutes and maintained for 1 hour. Afterward, the mixture was allowed to cool to room temperature naturally, and centrifuged twice with ethanol. Finally, the product was dissolved in 10 mL of hexane for use.

Synthesis of $NaYF_4$:$x$$Er^{3+}$/2$Ce^{3+}$@$NaYF_4$ core–shell nanoparticles. Firstly, the rare earth salt precursor was synthesized. 4 g of Yb_2O_3 was weighed and added to a three-neck flask along with equal amounts of deionized water and trifluoroacetic acid. The mixture was heated to 90 °C. Once the solution became clear, the reaction was continued for an additional half an hour. After this, nitrogen was continuously injected to remove the solvent and $Yb(TFA)_3$ powders were obtained. 5 mL of the prepared core, 0.5 mmol of $Yb(TFA)_3$, 1 mmol of Na$(TFA)_3$, 10 mL of OA, and 10 mL of ODE were added into a triple-neck flask. Nitrogen was continuously injected while stirring the mixture. The mixture was heated to 120 °C and this temperature was maintained for 30 minutes. Then, the temperature was increased to 300 °C over a period of 20 minutes and this temperature was held for 1 h. The mixture was naturally cooled to room temperature. Then, it was centrifuged, and the precipitate was washed twice with ethanol and then dissolved in 10 mL of hexane for use.

Synthesis of $NaYF_4$:$x$$Er^{3+}$/2$Ce^{3+}$@$NaYbF_4$@$NaYF_4$:$Yb^{3+}$/$Nd^{3+}$ core–shell–shell nanoparticles. The above steps were followed to obtain $Y(TFA)_3$ and $Nd(TFA)_3$ as well. The $NaYF_4$:Yb^{3+}/Nd^{3+} layers were grown on the core–shell nanoparticles by a similar method except for the different amounts of $Y(TFA)_3$, Yb $(TFA)_3$ and $Nd(TFA)_3$.

Synthesis of PAA-capped nanoprobes. 100 mg of nitrosonium tetrafluoroborate ($NOBF_4$) was dissolved in 5 mL of *N*,*N*-dimethylformamide (DMF). 2 mL of the core–shell–shell nanoparticles was added to the solution, and shaken thoroughly for 10 minutes. Next, 10 mL of hexane and 10 mL of toluene were added, and then the mixture was centrifuged. The precipitate was collected and dissolved in 5 mL of DMF. 0.3 g of PAA was added to the solution, and it was heated to 90 °C for 30 minutes, and then precipitated with acetone. The precipitate was collected and dissolved in 2 mL of PBS.

Animal experiments. Kunming mice were purchased from The Second Affiliated Hospital of Harbin Medical University. Animal procedures were performed in accordance with the guidelines of the Institutional Animal Care and Use Committee, Harbin Institute of Technology.

Conflicts of interest

There are no conflicts to declare.

Data availability

Data supporting the conclusions of this article have been included as part of the ESI.† Any additional data not included in the ESI,† which are associated with this study, are available from the authors upon reasonable request.

Acknowledgements

This work was supported by grants from the National Natural Science Foundation of China (Grant No. 51972084 and 52272270), the Key Technology Research and Industrialization Demonstration Project of Qingdao (Grant No. 25-1-1-gjgg-1-gx), the Outstanding Young Scholars Project of the Natural Science Foundation of Heilongjiang Province, China (Grant No. JJ2023JQ0025), the Opening Project of State Key Laboratory of Space Power Sources (Grant No. YF07050123F2531), the Young Scientist Workshop (Harbin Institute of Technology) (Grant No. AUGA5710094420), and the Fundamental Research Funds for the Central Universities, China (Grant No. AUGA5710052614 and HIT.OCEF.2023041).

References

1 M. Jia, X. Chen, R. Sun, D. Wu, X. Li, Z. Shi, G. Chen and C. Shan, Lanthanide-based ratiometric luminescence nanothermometry, *Nano Res.*, 2023, **16**, 2949–2967.
2 X. Di, D. Wang, Q. P. Su, Y. Liu, J. Liao, M. Maddahfar, J. Zhou and D. Jin, Spatiotemporally mapping temperature

dynamics of lysosomes and mitochondria using cascade organelle-targeting upconversion nanoparticles, *Proc. Natl. Acad. Sci. U. S. A.*, 2022, **119**, e2207402119.

3 C. D. S. Brites, R. Marin, M. Suta, A. N. Carneiro Neto, E. Ximendes, D. Jaque and L. D. Carlos, Spotlight on luminescence thermometry: basics, challenges, and cutting-edge applications, *Adv. Mater.*, 2023, **35**, 2302749.

4 Y. Shen, J. Lifante, I. Zabala-Gutierrez, M. de la Fuente-Fernández, M. Granado, N. Fernández, J. Rubio-Retama, D. Jaque, R. Marin, E. Ximendes and A. Benayas, Reliable and remote monitoring of absolute temperature during liver inflammation via luminescence-lifetime-based nanothermometry, *Adv. Mater.*, 2022, **34**, 2107764.

5 L. Pu, P. Li, J. Zhao, Y. Wang, D. Guo, L. Li, Z. Wang and H. Suo, Eu^{3+}-activated single-band ratiometric nanothermometry by lattice negative thermal expansion, *Laser Photonics Rev.*, 2023, **17**, 2200884.

6 H. D. A. Santos, E. C. Ximendes, M. C. Iglesias-de la Cruz, I. Chaves-Coira, B. del Rosal, C. Jacinto, L. Monge, I. Rubia-Rodríguez, D. Ortega, S. Mateos, J. García Solé, D. Jaque and N. Fernández, In vivo early tumor detection and diagnosis by infrared luminescence transient nanothermometry, *Adv. Funct. Mater.*, 2018, **28**, 1803924.

7 J. C. Martins, A. R. N. Bastos, R. A. S. Ferreira, X. Wang, G. Chen and L. D. Carlos, Primary luminescent nanothermometers for temperature measurements reliability assessment, *Adv. Photonics Res.*, 2021, **2**, 2000169.

8 A. Puccini, N. Liu and E. Hemmer, Lanthanide-based nanomaterials for temperature sensing in the near-infrared spectral region: illuminating progress and challenges, *Nanoscale*, 2024, **16**, 10975–10993.

9 M. Jia, M. Li, D. Li, X. Zhang and G. Chen, Excitation-power dependence of lanthanide-based ratiometric luminescent nanothermometry, *Nano Lett.*, 2024, **24**, 15450–15456.

10 S. Yu, J. Xu, X. Shang, W. Zheng, P. Huang, R. Li, D. Tu and X. Chen, A dual-excitation decoding strategy based on NIR hybrid nanocomposites for high-accuracy thermal sensing, *Adv. Sci.*, 2020, **7**, 2001589.

11 X. Qiu, Q. Zhou, X. Zhu, Z. Wu, W. Feng and F. Li, Ratiometric upconversion nanothermometry with dual emission at the same wavelength decoded via a time-resolved technique, *Nat. Commun.*, 2020, **11**, 4.

12 H. Huang, H. Tuxun, K. Zhong, J. Huang, H. Wei and B. Zhou, Enabling nonthermally coupled upconversion in a core–shell–shell nanoparticle for ultrasensitive nanothermometry and anticounterfeiting, *ACS Appl. Nano Mater.*, 2024, **7**, 7794–7801.

13 R. An, Y. Liang, R. Deng, P. Lei and H. Zhang, Hollow nanoparticles synthesized via Ostwald ripening and their upconversion luminescence-mediated Boltzmann thermometry over a wide temperature range, *Light: Sci. Appl.*, 2022, **11**, 217.

14 F. Vetrone, R. Naccache, A. Zamarrón, A. Juarranz de la Fuente, F. Sanz-Rodríguez, L. Martinez Maestro, E. Martín Rodriguez, D. Jaque, J. García Solé and J. A. Capobianco, Temperature sensing using fluorescent nanothermometers, *ACS Nano*, 2010, **4**, 3254–3258.

15 Y. Wang, L. Lei, E. Liu, Y. Cheng and S. Xu, Constructing highly sensitive ratiometric nanothermometers based on indirectly thermally coupled levels, *Chem. Commun.*, 2021, **57**, 9092–9095.

16 C. Mi, J. Zhou, F. Wang, G. Lin and D. Jin, Ultrasensitive ratiometric nanothermometer with large dynamic range and photostability, *Chem. Mater.*, 2019, **31**, 9480–9487.

17 L. Yan, J. Huang, Z. An, Q. Zhang and B. Zhou, Activating ultrahigh thermoresponsive upconversion in an erbium sublattice for nanothermometry and information security, *Nano Lett.*, 2022, **22**, 7042–7048.

18 D. Li, M. Jia, T. Jia and G. Chen, Ultrasensitive NIR-II ratiometric nanothermometers for 3D in vivo thermal imaging, *Adv. Mater.*, 2024, **36**, 2309452.

19 B. del Rosal, E. Carrasco, F. Ren, A. Benayas, F. Vetrone, F. Sanz-Rodríguez, D. Ma, Á. Juarranz and D. Jaque, Infrared-emitting QDs for ehermal eherapy with real-time subcutaneous temperature feedback, *Adv. Funct. Mater.*, 2016, **26**, 6060–6068.

20 M. Quintanilla, M. Henriksen-Lacey, C. Renero-Lecuna and L. M. Liz-Marzán, Challenges for optical nanothermometry in biological environments, *Chem. Soc. Rev.*, 2022, **51**, 4223–4242.

21 C. Mi, X. Zhang, C. Yang, J. Wu, X. Chen, C. Ma, S. Wu, Z. Yang, P. Qiao, Y. Liu, W. Wu, Z. Guo, J. Liao, J. Zhou, M. Guan, C. Liang, C. Liu and D. Jin, Bone disease imaging through the near-infrared-II window, *Nat. Commun.*, 2023, **14**, 6287.

22 Y. Zhong, Z. Ma, F. Wang, X. Wang, Y. Yang, Y. Liu, X. Zhao, J. Li, H. Du, M. Zhang, Q. Cui, S. Zhu, Q. Sun, H. Wan, Y. Tian, Q. Liu, W. Wang, K. C. Garcia and H. Dai, In vivo molecular imaging for immunotherapy using ultra-bright near-infrared-IIb rare-earth nanoparticles, *Nat. Biotechnol.*, 2019, **37**, 1322–1331.

23 M. Zhang, J. Yue, R. Cui, Z. Ma, H. Wan, F. Wang, S. Zhu, Y. Zhou, Y. Kuang, Y. Zhong, D.-W. Pang and H. Dai, Bright quantum dots emitting at ~1,600 nm in the NIR-IIb window for deep tissue fluorescence imaging, *Proc. Natl. Acad. Sci. U. S. A.*, 2018, **115**, 6590–6595.

24 H. D. A. Santos, I. Zabala Gutiérrez, Y. Shen, J. Lifante, E. Ximendes, M. Laurenti, D. Méndez-González, S. Melle, O. G. Calderón, E. López Cabarcos, N. Fernández, I. Chaves-Coira, D. Lucena-Agell, L. Monge, M. D. Mackenzie, J. Marqués-Hueso, C. M. S. Jones, C. Jacinto, B. del Rosal, A. K. Kar, J. Rubio-Retama and D. Jaque, Ultrafast photochemistry produces superbright short-wave infrared dots for low-dose in vivo imaging, *Nat. Commun.*, 2020, **11**, 2933.

25 E. C. Ximendes, W. Q. Santos, U. Rocha, U. K. Kagola, F. Sanz-Rodríguez, N. Fernández, A. d. S. Gouveia-Neto, D. Bravo, A. M. Domingo, B. del Rosal, C. D. S. Brites, L. D. Carlos, D. Jaque and C. Jacinto, Unveiling in vivo subcutaneous thermal dynamics by infrared luminescent nanothermometers, *Nano Lett.*, 2016, **16**, 1695–1703.

26 A. Skripka, A. Benayas, R. Marin, P. Canton, E. Hemmer and F. Vetrone, Double rare-earth nanothermometer in aqueous media: opening the third optical transparency window to temperature sensing, *Nanoscale*, 2017, **9**, 3079–3085.

27 K. Maciejewska, A. Bednarkiewicz and L. Marciniak, The influence of the Er^{3+} dopant concentration in $LaPO_4$:Nd^{3+}, Er^{3+} on thermometric properties of ratiometric and kinetic-based luminescent thermometers operating in NIR II and NIR III optical windows, *Phys. B*, 2021, **620**, 413247.

28 Y. Wu, F. Li, Y. Wu, H. Wang, L. Gu, J. Zhang, Y. Qi, L. Meng, N. Kong, Y. Chai, Q. Hu, Z. Xing, W. Ren, F. Li and X. Zhu, Lanthanide luminescence nanothermometer with working wavelength beyond 1500 nm for cerebrovascular temperature imaging in vivo, *Nat. Commun.*, 2024, **15**, 2341.

29 S. Liu, Z. An, J. Huang and B. Zhou, Enabling efficient NIR-II luminescence in lithium-sublattice core—shell nanocrystals towards Stark sublevel based nanothermometry, *Nano Res.*, 2023, **16**, 1626–1633.

30 E. C. Ximendes, U. Rocha, T. O. Sales, N. Fernández, F. Sanz-Rodríguez, I. R. Martín, C. Jacinto and D. Jaque, In vivo subcutaneous thermal video recording by supersensitive infrared nanothermometers, *Adv. Funct. Mater.*, 2017, **27**, 1702249.

31 H. Li, M. Tan, X. Wang, F. Li, Y. Zhang, L. Zhao, C. Yang and G. Chen, Temporal multiplexed in vivo upconversion imaging, *J. Am. Chem. Soc.*, 2020, **142**, 2023–2030.

32 L. Wu, M. Jia, D. Li and G. Chen, Shell engineering on thermal sensitivity of lifetime-based NIR nanothermometers for accurate temperature measurement in murine internal liver organ, *Nano Lett.*, 2023, **23**, 2862–2869.

33 D. Li, M. Jia, J. Du, Y. Li, T. Jia and G. Chen, Optomagnetic heater-thermometer nanoplatform for tumor magnetothermal therapy with operando temperature feedback, *ACS Nano*, 2025, **19**, 8328–8337.

34 M. Kong, Y. Gu, Y. Chai, J. Ke, Y. Liu, X. Xu, Z. Li, W. Feng and F. Li, Luminescence interference-free lifetime nanothermometry pinpoints in vivo temperature, *Sci. China: Chem.*, 2021, **64**, 974–984.

35 Ł. Marciniak, A. Bednarkiewicz, M. Stefanski, R. Tomala, D. Hreniak and W. Strek, Near infrared absorbing near infrared emitting highly-sensitive luminescent nanothermometer based on Nd^{3+} to Yb^{3+} energy transfer, *Phys. Chem. Chem. Phys.*, 2015, **17**, 24315–24321.

36 Y. Huang, J. Hu, Y. Guo, Z. Wang, F. Lin and H. Zhu, Effect of –OH on the thermal enhancement properties of NIR-II lanthanide-doped nanoparticles in water, *Inorg. Chem. Front.*, 2024, **11**, 3063–3072.

37 Y. Sun, M. Kong, J. Ke, W. Yuan, C. Wen, Y. Gu, S. Luo and W. Feng, Nanothermometer for In Vivo Temperature detection with high spatial resolution based on core–shell rare earth nanoparticles, *ACS Appl. Nano Mater.*, 2023, **6**, 23173–23183.

38 C. Li, J. Ge, D. Song, T. Liang and Z. Li, Activatable near-infrared IIb rare-earth nanoprobe for early monitoring chemotherapy-induced liver injury, *Adv. Funct. Mater.*, 2025, 2502077.

39 H. D. A. Santos, D. Ruiz, G. Lifante, C. Jacinto, B. H. Juarez and D. Jaque, Time resolved spectroscopy of infrared emitting Ag_2S nanocrystals for subcutaneous thermometry, *Nanoscale*, 2017, **9**, 2505–2513.

40 J. Zhao, J. Chang, N. Wang, P. Zhao, M. Zhu, Y. Liu, D. Guo, Y. Wang, P. Li, Z. Wang and H. Suo, Thermal enhancement of Er^{3+} NIR-II luminescence by Ho^{3+}-mediated energy-trapping in negative thermal expansion nanocrystals, *Laser Photonics Rev.*, 2024, **18**, 2400151.

41 Q. Hu, N. Kong, Y. Chai, Z. Xing, Y. Wu, J. Zhang, F. Li and X. Zhu, A lanthanide nanocomposite with cross-relaxation enhanced near-infrared emissions as a ratiometric nanothermometer, *Nanoscale Horiz.*, 2022, **7**, 1177–1185.

42 X. Yuan, E. Cui, K. Liu, Y. Jiang, X. Yang, J. Tang, L. Yang, X. Liao, Y. Zhao, W. Sun, Y. Liu and J. Liu, Lanthanide-doped $NaYF_4$ near-infrared-II nanothermometers for deep tissue temperature sensing, *Ceram. Int.*, 2022, **48**, 35141–35149.

43 P. Cortelletti, A. Skripka, C. Facciotti, M. Pedroni, G. Caputo, N. Pinna, M. Quintanilla, A. Benayas, F. Vetrone and A. Speghini, Tuning the sensitivity of lanthanide-activated NIR nanothermometers in the biological windows, *Nanoscale*, 2018, **10**, 2568–2576.